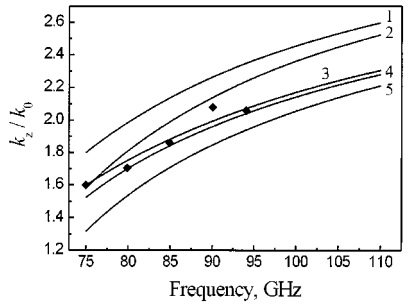

Fig. 4. k_z/k_0 of a DRW made of uniaxial anisotropic materials with cross dimensions of 1.0 × 0.5 mm^2. (1) $\varepsilon_{r\perp} = 11.56, \varepsilon_{r||} = 11.56$. (2) $\varepsilon_{r\perp} = 11.56, \varepsilon_{r||} = 9.39$. (3) Calculated experimental based on the from phase measurement results. (4) $\varepsilon_{r\perp} = 9.39, \varepsilon_{r||} = 11.56$. (5) $\varepsilon_{r\perp} = 9.39, \varepsilon_{r||} = 9.39$; ◇—directly measured experimental points.

$\Delta k = \Delta\phi/L$, where $\Delta\phi$ is the phase-shift change when frequency changes by a small step to the next point, and Δk is a change in the propagation constant in the dielectric waveguide. After obtaining the wavelength at one point by using the phase data, one can calculate the propagation constants at other frequencies (Fig. 4, curve 3). For comparison, the normalized propagation constant measurements were repeated at 80, 85, 90, and 94 GHz. The results are shown in Fig. 4.

One can see in Fig. 4 (curves 3 and 4) that the modified Marcatili method for the sapphire DRW gives a good agreement with the experimental data. The fact that the theoretical curve lies below the experimental one can be explained by the approximative nature of the Marcatili method.

Comparing curve 1 with 2 and 4 with 5, one can see that the anisotropy changes the propagation characteristic considerably. The dispersion is increased, as with curve 2, when $\varepsilon_{||}$ is smaller than $\varepsilon_{\perp}$ or decreased when $\varepsilon_{||}$ is larger than $\varepsilon_{\perp}$, as with curve 4. The latter could be explained as follows. When the frequency is very high, there is almost no longitudinal electric-field component, and the propagation constant results mainly from $\varepsilon_{\perp}$. When the frequency drops, the longitudinal component of the electric field becomes larger; therefore, the effect of larger $\varepsilon_{||}$ becomes stronger and, thus, k_z/k_0 increases. Similarly, one can explain why the dispersion seen in the case of curve 2 is stronger.

V. Conclusion

In this paper, we have presented the modified Marcatili method for the calculation of a rectangular DRW made of uniaxial electrically anisotropic dielectric material with the optical axis coinciding with the axis of the DRW. In a more general case (arbitrary direction of the optical axis, anisotropic permeability, etc.), equations similar to (2) may be derived and solved using this approach. Equations have been derived without guessing the field distribution. This method is relatively simple and sufficiently accurate for a DRW operating far from the cutoff, as with the original Marcatili method for the isotropic case. The propagation constant of an anisotropic sapphire DRW oriented along the optical axis has been measured. Experimental results show a good agreement with those calculated by our approach.

References

[1] A. Sudbø, "Why are the accurate computations of mode fields in rectangular dielectric waveguides difficult?," *J. Lightwave Technol.*, vol. 10, pp. 418–419, Apr. 1992.

[2] T. Itoh, *Numerical Techniques for Microwave and Millimeter-Wave Passive Structures*. New York: Wiley, 1989.

[3] S. Garcia, T. Hung-Bao, R. Martin, and B. Olmedo, "On the application of finite methods in time domain to anisotropic dielectric waveguides," *IEEE Trans. Microwave Theory Tech.*, vol. 44, pp. 2195–2206, Dec. 1996.

[4] E. A. J. Marcatili, "Dielectric rectangular waveguide and directional coupler for integrated optics," *Bell Syst. Tech. J.*, vol. 48, pp. 2071–2102, 1969.

[5] R. M. Knox and P. P. Toulios, "Integrated circuits for the millimeter through optical frequency range," in *Proc. Submillimeter Waves Symp.*, York, NY, 1970, pp. 497–516.

[6] M. I. Oksanen, S. A. Tretyakov, and I. V. Lindell, "Vector circuit theory for isotropic and chiral slabs," *J. Electromagn. Waves Applicat.*, vol. 4, pp. 613–634, 1990.

[7] D. V. Lioubtchenko, S. Dudorov, J. Mallat, J. Tuovinen, and A. V. Räisänen, "Low loss sapphire waveguides for 75–110 GHz frequency range," *IEEE Microwave Wireless Comp. Lett.*, vol. 11, pp. 252–254, June 2001.

[8] T. Itoh, "Dielectric waveguide-type millimeter-wave integrated circuits," in *J. Infrared and Millimeter Waves*, K. J. Button and J. C. Wiltse, Eds. New York: Academic, 1981, vol. 4, ch. 5, pp. 199–273.

[9] Y. Kobayashi and T. Tomohiro, "Resonant modes in shielded uniaxial-anisotropic dielectric rod resonators," *IEEE Trans. Microwave Theory Tech.*, vol. 41, pp. 2198–2205, Dec. 1993.

[10] V. V. Parshin, "Dielectric materials for gyrotron output windows," *Int. J. Infrared Millim. Waves*, vol. 15, pp. 339–348, Feb. 1994.

Microwave I–Q Vector Modulator Using a Simple Technique for Compensation of FET Parasitics

Mitchai Chongcheawchamnan, Sawat Bunnjaweht, David Kpogla, Dongwook Lee, and Ian D. Robertson

***Abstract*—The analysis and design of an improved technique for the realization of vector modulators using analog reflection-type circuits are presented. The analysis focuses on the detrimental effect that the parasitic elements of the FET variable-resistance elements have on the 360° phase and amplitude control. It is shown that a simple circuit technique can be used to compensate for the parasitic effects and achieve a near-ideal constellation. Compared with the balanced structure, the proposed technique leads to a much smaller circuit area and does not require additional complementary control signals. This makes it better suited to commercial wireless applications where low cost is paramount. Simulation and experimental results for an L-band prototype are presented.**

***Index Terms*—Cold FET, parasitic elements, vector modulator.**

I. Introduction

The vector modulator plays an increasingly important role in modern communication systems. For example, in a linearized amplifier system, a vector modulator can provide simultaneous phase and amplitude tuning, rather than applying a variable attenuator cascaded with a variable phase shifter [1]. High-performance vector modulators can be used as the electronic controllable elements for an adaptive beamforming network in phased-array antenna applications [2]. In digital communication applications, a vector modulator is widely

Manuscript received March 26, 2001. This work was supported by the Mahanakorn University of Technology and by RF Hitec Inc.

M. Chongcheawchamnan, S. Bunnjaweht, D. Kpogla, and I. D. Robertson are with the School of Electronic Engineering and Mathematics Department, University of Surrey, Guildford, Surrey, U.K.

D. Lee is with Nextec Microwave and RF Inc., Santa Clara, CA 95050 USA.

Publisher Item Identifier S 0018-9480(02)05215-8.

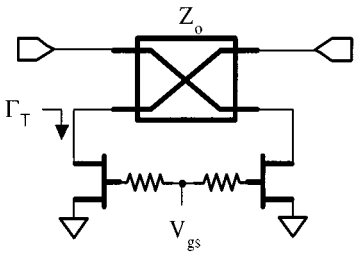

Fig. 1. Schematic diagram of an analog RTA.

used to generate I–Q modulated signals or to perform frequency translation.

Traditionally, a vector modulator can be realized by two main approaches in microwave and millimeter-wave applications. The first approach is based on two orthogonal bi-phase modulators combined with a 3-dB power combiner. Realizing a circuit with this technique has a 3-dB inherent loss penalty. The second approach is based on a variable attenuator and a 360° variable phase shifter. Though the second approach is attractive in terms of having no inherent insertion loss, a high-performance variable attenuator with a constant phase and a phase shifter with constant insertion loss are needed. These are notoriously difficult to design, and laborious amplitude and phase control schemes are often required for such a modulator. Hence, the first approach is more attractive in terms of realization, especially in microwave and milimeter-wave applications since the system is composed of a single circuit block, namely the bi-phase variable attenuator.

The analog reflection-type attenuator (RTA) was first proposed and applied to a vector modulator by Devlin and Minnis [3]. A variable resistance reflection termination is used so that the attenuation level can be controlled. The MESFET device is preferred over a p-i-n diode because of its near-zero dc control power and widespread availability in foundry processes. However, it has a smaller dynamic range of resistance and larger parasitic elements. The balanced, or push–pull, configuration is one way to remove the amplitude and phase errors caused by the active device parasitics [4]. This structure employs a second attenuator operated in antiphase, giving good constellation symmetry, but the chip area is more than doubled.

In this paper, a simple technique of compensating for the FET parasitics is presented that achieves improved constellation accuracy without resorting to a balanced topology. First, the parasitic elements of the FET and their effects on the modulator are analyzed in Section II. Section III then describes the proposed simplified technique and analyzes the improvement in constellation symmetry between zero bias and pinchoff. Based on the proposed technique, the experimental results on a vector modulator demonstrated practically at 1.8 GHz are described in Section IV.

II. Analysis of FET Parasitic Effects on the RTA

Fig. 1 shows the configuration of the RTA. The cold FETs are used as reflection terminations, which theoretically provide an ideal variable resistor [5]. In practice, parasitic elements (junction capacitances, feed inductance, etc.) introduce phase and amplitude error, which restricts the application of the vector modulator. Previously, the technique reported to overcome this problem is a balanced structure. Compared with the RTA in Fig. 1, three additional hybrid couplers are required and an additional complementary baseband control $\bar{I}$ is required. Since circuit complexity increases, a larger area for the circuit is needed. To implement a vector modulator, the balanced topology requires nine hybrid couplers, one Wilkinson divider, eight active devices, and four baseband signal channels. Thus, a large chip area is needed for monolithic microwave integrated circuit (MMIC) realization which, in turn,

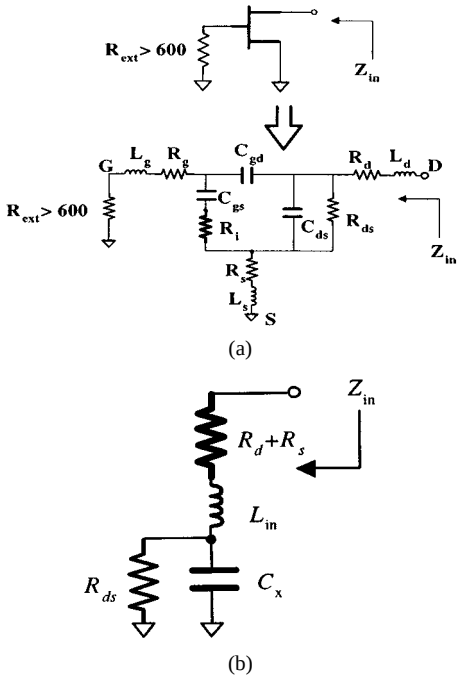

Fig. 2. Circuit diagram of: (a) small-signal model of MESFETs and (b) equivalent circuit of a cold FET.

results in higher manufacturing costs. Moreover, the larger number of signal controlling channels, which are $I, Q, \bar{I}$, and $\bar{Q}$, increases the complexity of the baseband circuitry. For example, a four-channel D-to-A converter is needed instead of the two-channel one needed for a conventional I–Q modulator. Also, while the vector modulator based on the balanced structure theoretically achieves only 3-dB insertion loss, in practice, the insertion loss can be increased considerably due to the combined losses of those nine hybrid couplers. The s_{21} of this variable attenuator is directly related to Γ_T, while s_{11} and s_{22} are perfectly matched to Z_o. In this paper, we study the effect of transistor parameters on the modulator performance by assuming that the quadrature hybrid coupler is ideal. Fig. 2(a) shows the cold FET and its equivalent small-signal circuit. The transistors are operated at zero drain–source voltage. The gate–drain and gate–source capacitances $(C_{\rm gd}, C_{\rm gs})$, which represent the variation in the depletion charge with respect to the applied voltage, are equal because the depletion channel is symmetrical at this biasing point [6], i.e., $C_{\rm gd} = C_{\rm gs}$. Due to this, the device model shown in Fig. 2(a) can be reduced to the simplified equivalent circuit shown in Fig. 2(b). Let

$$C_x = C_{\rm ds} + \frac{C_{\rm gd}}{2}. \tag{1}$$

The input impedance $Z_{\rm in}$ of the cold-FET device is given by

$$Z_{\rm in} = R_{\rm in} + jX_{\rm in} \tag{2}$$

$$R_{\rm in} = R_d + R_s + \frac{R_{\rm ds}}{1 + (\omega R_{\rm ds} \cdot C_x)^2} \tag{3}$$

$$L_{\rm in} = L_d + L_s \tag{4}$$

$$C_{\rm in} = \frac{1 + \omega^2 R_{\rm ds}^2 C_x^2}{\omega^2 R_{\rm ds}^2 C_x} \tag{5}$$

where R_d, R_s and $R_{\rm ds}$ are the drain, source, and drain–source resistance, respectively. R_s and R_d represent the ohmic contacts and any bulk resistances leading up to the active channel. These two resistances are on the order of 1 Ω [6]. The drain and source inductance (L_d, L_s), primarily resulting from contact pads, are typically less than 10 pH [6].

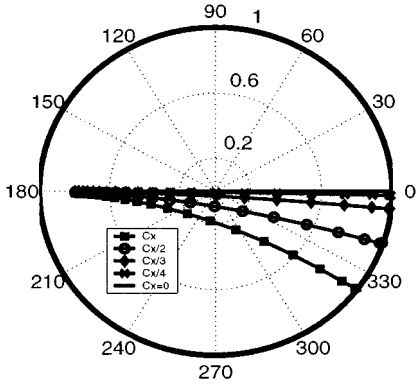

Fig. 3. Effect of parasitic capacitances on Γ_T.

The drain–source capacitance ($C_{\rm ds}$) is related to the geometric capacitance between the source and drain electrodes.

The gate resistance (R_g) and inductance (L_g) result from the metallization of the gate Schottky contact and metal contact pad. They have no effect on $Z_{\rm in}$ since they are absorbed by a large gate biasing resistor, which treats the transistor gate as an open circuit. Consequently, only the two model elements, i.e., $C_{\rm gd}$ and $R_{\rm ds}$, are bias-dependent cold-FET parameters.

From (3), the fixed parasitic resistances directly affect $R_{\rm in}$ and simply lead to an increase in insertion loss. The effect of parasitic inductance dominates as the applied bias is approaching zero since $C_{\rm in}$ becomes large. Since these parasitic inherent effects are small, we assume that these parameters are negligible. The equivalent circuit of the cold FET will be reduced to a parallel circuit form ($R_{\rm ds}$ and C_x). The input impedance of this circuit (2) can be written as

$$Z_{\rm in} = \frac{1}{1+(\omega R_{\rm ds}C_x)^2}\left(R_{\rm ds} - j\omega R_{\rm ds}^2 C_x\right). \tag{6}$$

Consequently, Γ_T is given by

$$|\Gamma_T| = \sqrt{\frac{(Z_o - R_{\rm ds})^2 + (\omega R_{\rm ds}C_x Z_o)^2}{(Z_o + R_{\rm ds})^2 + (\omega R_{\rm ds}C_x Z_o)^2}} \tag{7}$$

$$\angle\Gamma_T = \tan^{-1}\frac{2\omega R_{\rm ds}^2 C_x Z_o}{(Z_o^2 - R_{\rm ds}^2) + (\omega R_{\rm ds}C_x Z_o)^2}. \tag{8}$$

Fig. 3 shows the effect of C_x on the characteristic of Γ_T for an FET with the parameters listed in Table I. It is shown in the result that the existence of capacitance causes the phase trajectory of Γ_T at pinchoff voltage ($V_{\rm TO}$) to deviate from the real axis. Hence, 180° phase difference cannot be achieved. This Γ_T characteristic is not suitable for a bi-phase and vector modulator implementation. The bias-dependent model parameter is now considered. Here, we use the Curtice FET model to analyze the cold FET. It is shown that $R_{\rm ds}$ increases when $V_{\rm gs}$ is more negative since the channel is narrowed. Conversely, $C_{\rm gd}$ is decreased when $V_{\rm gs}$ is more negative since the charge in the depletion region is smaller.

III. Proposed Technique to Improve the RTA

The technique presented here to compensate for the FET parasitics in the vector modulator has two parts. Firstly, a series inductance is introduced, which moves the left half of the Γ_T trace to the upper half of the Smith chart, while only causing a small change in Γ_T at the bias near to $V_{\rm TO}$. By optimum choice of this added inductance, the phase difference can be set to 180°. Secondly, a shunt resistor is introduced to equalize the magnitudes of Γ_T at $V_{\rm gs} = 0$ and pinchoff.

TABLE I
List of Extracted Curtice Model Parameters of CFY30 FET

Parameter	Value
α	0.285
β	0.1541
V_{TO}	−1.9
C_{gd0}	1.891 pF
C_{ds}	0.1 pF
V_{bi}	0.7

A. Effect of External Inductance on $|\Gamma_T|$

If an external series inductance L_x is deliberately applied, connected at either the drain or source, then Γ_T is obtained as follows:

$$|\Gamma_T| = \sqrt{\frac{(Z_o - R_{\rm ds})^2 + (\omega R_{\rm ds}C_x Z_o)^2 + \Delta}{(Z_o + R_{\rm ds})^2 + (\omega R_{\rm ds}C_x Z_o)^2 + \Delta}} \tag{9}$$

$$\angle\Gamma_T = \tan^{-1}\frac{2\omega Z_o\left[R_{\rm ds}^2 C_x - L_x\cdot\left(1+\omega^2 R_{\rm ds}^2 C_x^2\right)\right]}{(Z_o^2 - R_{\rm ds}^2) + (\omega R_{\rm ds}C_x Z_o)^2 - \Delta} \tag{10}$$

where $\Delta = \omega^2[L_x^2(1+(\omega R_{\rm ds}C_x)^2) - 2R_{\rm ds}^2 C_x L_x]$.

The inductance L_x is used to control Γ_T at $V_{\rm gs} = 0$, and causes only a small change of Γ_T when the FET is biased near pinchoff. In this section, the sensitivity of $|\Gamma_T|$ with L_x is investigated. If the sensitivity of $|\Gamma_T|$ is very small, this implies that the effect of L_x on $|\Gamma_T|$ is also negligible. The sensitivity definition is applied to prove this for the bias voltage near pinchoff. Let $S_x^{f[x]}$ be the sensitivity of a parameter x to a function $f[x]$, which is defined as follows [8]:

$$S_x^{f[x]} = \frac{\partial \ln f[x]}{\partial \ln x}. \tag{11}$$

Hence, applying (11) to $|\Gamma_T|$ with respect to L_x, we obtain the sensitivity function shown in (14). Thus, for a bias point that is very close to pinchoff ($R_{\rm ds} \to \infty$)

$$S_{L_x}^{|\Gamma_T|}(V_{\rm gs} = V_{\rm TO}) \equiv \lim_{R_{\rm ds}\to\infty} S_{L_x}^{|\Gamma_T|} = 0. \tag{12}$$

Also, at zero bias, $R_{\rm ds}$ is very small ($R_{\rm ds} \to 0$). Hence, (13) and (14), shown at the bottom of the following page.

This implies that adding L_x to the termination circuit has no effect on $|\Gamma_T|$ at zero and pinchoff bias points.

B. Optimum L_x for a Bi-Phase Modulator

Applying L_x causes a significant change in $\angle\Gamma_T$ when $V_{\rm gs}$ is near zero. The effect of L_x can be predicted by considering (4), which makes the $|\Gamma_T|$ trace move upward to the upper plane of the Smith chart. We study this by applying different values of L_x to the device (CFY30) (Table I). Fig. 4 shows the Γ_T obtained by applying values between $L_x = 0$ and $L_x = 3$ nH. It is shown that the positions of Γ_T at $V_{\rm gs} \to 0$ depend on the value of L_x, and $|\Gamma_T|$ is also improved due to the reduction in $X_{\rm in}$.

The optimum value of L_x is obtained by considering the phase difference of Γ_T, which should be 180° between the two extreme biasing points, i.e., $V_{\rm gs} = 0$ and near pinchoff voltage, i.e.,

$$(\angle\Gamma_T)_{V_{\rm gs}=0} - (\angle\Gamma_T)_{V_{\rm gs}\to V_{\rm TO}} = \pi. \tag{15}$$

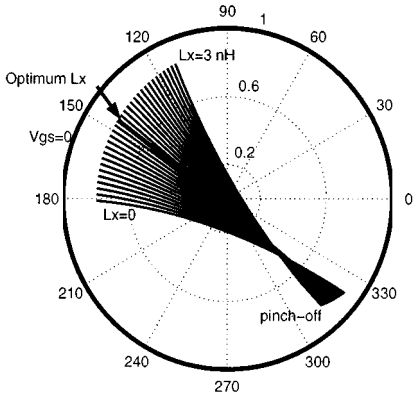

Fig. 4. Effect of additional series inductance L_x on Γ_T.

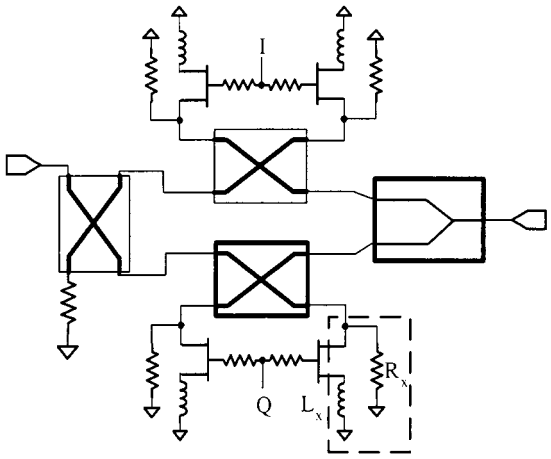

Fig. 5. Proposed vector modulator.

At $V_{\rm gs} = 0$, the value of parasitic resistance and drain–source resistance are very small compared with the reactance of the external inductance. Hence, we can simplify $\angle\Gamma_T$ for this case as

$$(\angle\Gamma_T)_{V_{\rm gs}=0} \approx \tan^{-1}\frac{-2\omega Z_o L_x}{Z_o^2 - (\omega L_x)^2}. \tag{16}$$

As the bias is close to pinchoff, the reactance resulting from L_x is very small when compared with $R_{\rm ds}$ and ωC_x; hence, (9) becomes

$$(\angle\Gamma_T)_{V_{\rm gs}-V_{\rm TO}} \approx \tan^{-1}\frac{2\omega Z_o C_x R_{\rm ds}^2}{Z_o^2 - R_{\rm ds}^2 + \omega R_{\rm ds} C_x Z_o^2}. \tag{17}$$

Substituting (17) and (16) into the condition defined in (15), we then obtain the optimum value of L_x, which provides a 180° phase difference of Γ_T as follows.

Since $R_{\rm ds}$ at pinchoff is very large, we can then approximate (19) as follows:

$$L_{xa} \approx \lim_{R_{\rm ds}\to\infty} L_x = \frac{\sqrt{1 + 4\omega^2 Z_o^2 C_x (V_{\rm TO})^2} - 1}{2C_x(V_{\rm TO}))\omega^2}. \tag{18}$$

Fig. 4 shows that the best phase trajectory is obtained with $L = 1.4$ nH, which agrees with the optimum value of 1.33 nH obtained from (18). It is also evident from Fig. 4 that the extra inductance provides a better dynamic range of attenuation since Γ_T now passes very close to the center point of the Smith chart.

C. Shunt Resistor to Correct Amplitude Asymmetry

The amplitude imbalance between $V_{\rm gs} = 0$ and $V_{\rm gs} = V_{\rm TO}$ occurs due to the existence of small parasitic resistances at the drain and source, which will dominate when the FET is zero biased. Normally, the $|\Gamma_T|$ at $V_{\rm gs} = 0$ is smaller than $|\Gamma_T|$ near pinchoff. To correct this, a shunt resistor is applied at the drain to reduce the overall impedance when the FET is biased near to pinchoff. This decreases the $|\Gamma_T|$ at pinchoff to the $|\Gamma_T|$ value obtained when zero gate–source bias is applied. The full schematic diagram of the proposed improved technique for the vector modulator is shown in Fig. 5. This modified RTA gives improved performance and can be used as a bi-phase amplitude modulator and in a vector modulator, without resorting to the large balanced topology.

Applying this structure to a complete vector modulator, the full 360° phase rotation is achieved with very few additional components. It should be noted that the nonlinear phase and amplitude tuning characteristic can be corrected. One possible approach to correct this problem is by applying a predistortion function, which is straightforward to implement in software or by applying predistortion circuitry.

IV. Measured Performance

The implementation is performed with a packaged CFY30 device, which has $f_{\max} = 12$ GHz. All the circuits are realized on a printed circuit board (PCB) using microstrip transmission lines. The substrate is epoxy glass ($h = 1.6$ mm, $\epsilon_r = 4.55$, FR-4). All hybrid couplers are realized using two 8.4-dB couplers connected in a tandem fashion [10] to obtain a 3-dB coupler. A complete vector modulator based on the proposed technique is constructed. Fig. 6 shows the photograph of the vector modulator. All the lumped elements on the PCB are surface mount (type 0805). The small external inductors are realized by a microstrip line and taking the via-hole connecting line into account (1 mm ≈ 1 nH). The parasitic inductance from via-holes is minimized by using parallel via-holes.

The measurement is performed with an HP 8510C network analyzer test system. The s_{11} and s_{22} of the vector modulator are well below −15 dB at 1.8 GHz (see (19) at the bottom of the following page).

Fig. 7 shows the measurement results of the vector modulator using the proposed technique. The dynamic range of this vector modulator is from −5.2 to −60 dB and a full 360° phase rotation is achieved. The amplitude and phase imbalance at 1.8 GHz are well below 0.4 dB and 3°. The amplitude and relative phase frequency response of the proposed vector modulator for eight different bias points are shown in Fig. 8(a) and (b), respectively.

$$S_{L_x}^{|\Gamma_T|}(V_{\rm gs} = 0) \equiv \lim_{R_{\rm ds}\to 0} S_{L_x}^{|\Gamma_T|} = 0 \tag{13}$$

$$S_{L_x}^{|\Gamma_T|} = \frac{4Z_o R_{\rm ds}\omega^2\left[L_x\left(1 + \omega^2 R_{\rm ds}^2 C_x^2\right) - R_{\rm ds}^2 C_x\right)\right]}{\left((Z_o - R_{\rm ds})^2 + (\omega R_{\rm ds} C_x Z_o)^2 + \Delta\right)\cdot\left((Z_o + R_{\rm ds})^2 + (\omega R_{\rm ds} C_x Z_o)^2 + \Delta\right)} \tag{14}$$

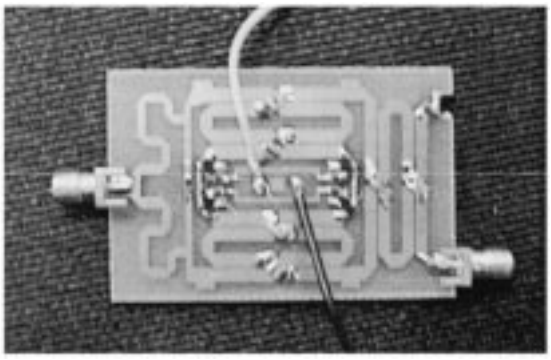

Fig. 6. Photograph of the improved vector modulator.

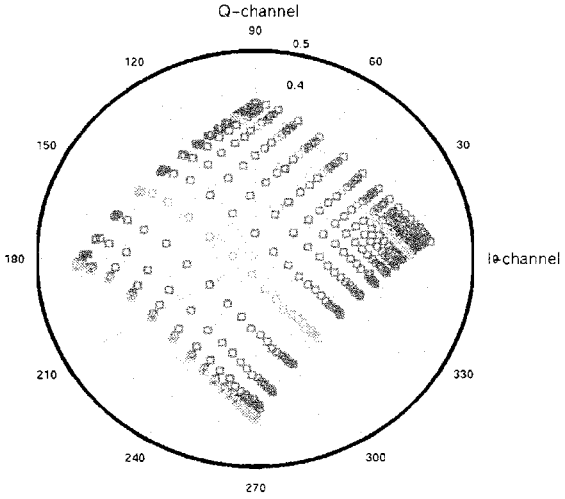

Fig. 7. Measurement result of s_{21} of a vector modulator using the proposed technique.

V. Conclusion

The analysis of the effect of the cold-FET parasitic elements on the bi-phase modulator and vector modulator has been described. It has been shown that the junction capacitances cause the Γ_T to deviate from the real axis of the Smith chart. A new simple technique to correct for phase distortion and extend the dynamic range of attenuation has been developed. The asymmetry of modulator insertion loss between the two bias extremes, i.e., $V_{\rm gs} = 0$ and near pinchoff, is also corrected by simply adding a shunt resistor. Simulation and experimental results demonstrate the effectiveness of the proposed technique.

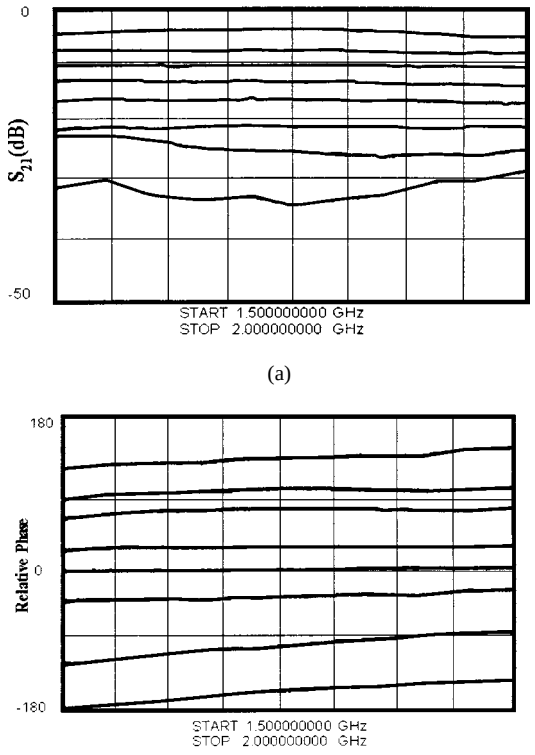

Fig. 8. (a) Amplitude and (b) relative phase response of the proposed vector modulator.

References

[1] W. T. Thornton and L. E. Larson, "An improved 5.7 GHz ISM-band feedforward amplifier utilizing vector modulators for phase and attenuation control," *Microwave J.*, vol. 42, no. 12, pp. 96–106, Dec. 1999.

[2] I. D. Robertson, *MMIC Design*. London, U.K.: IEE, 1995.

[3] L. M. Devlin and B. J. Minnis, "A versatile vector modulator design for MMIC," in *IEEE MTT-S Int. Microwave Symp. Dig.*, 1990, pp. 519–522.

[4] A. E. Ashitiani, S. Nam, A. d'Espona, S. Lucyszyn, and I. D. Robertson, "Direct multilevel carrier modulation using millimeter-wave balanced vector modulators," *IEEE Trans. Microwave Theory Tech.*, vol. 46, pp. 2611–2219, Dec. 1998.

[5] R. Anholt and S. Swirhum, "Equivalent-circuit parameter extraction for cold GaAs MESFET's," *IEEE Trans. Microwave Theory Tech.*, vol. 39, pp. 1243–1247, July 1991.

[6] J. M. Golio, *Microwave MESFET's and HEMTs*. Norwood, MA: Artech House, 1991.

[7] S. Lucyszyn and I. D. Robertson, "Analog reflection topology building blocks for microwave signal processing applications," *IEEE Trans. Microwave Theory Tech.*, vol. 43, pp. 601–611, Mar. 1995.

[8] G. Daryanani, *Principle of Active Network Synthesis and Design*. New York: Wiley, 1976.

[9] H. Statz, P. Newman, I. W. Smith, R. A. Pucel, and H. A. Haus, "GaAs FET device and circuit simulation in SPICE," *IEEE Trans. Electron Devices*, vol. ED-34, pp. 160–169, Feb. 1987.

[10] R. Mongia, I. Bahl, and P. Bhartia, *RF and Microwave Coupled-Line Circuits*. Norwood, MA: Artech House, 1999.

$$L_x = \frac{1}{2}\frac{Z_o^2(1+\omega R_{\rm ds}C_x) - R_{\rm ds}^2 + \sqrt{Z_o^4(1+\omega R_{\rm ds}C_x)^2 + R_{\rm ds}^4(1+4\omega^2 Z_o^2 C_x^2) - 2\omega R_{\rm ds}^3 C_x Z_o^2 - 2R_{\rm ds}^2 Z_o^2}}{(\omega R_{\rm ds})^2 C_x} \tag{19}$$